Numerical Analysis of an Active Thermomagnetic Device for Thermal Energy Harvesting

Makita R. Phillips[1]
Department of Mechanical and
Aerospace Engineering,
UCLA,
46-147N EIV,
Los Angeles, CA 90095-1597

Gregory P. Carman
Department of Mechanical and
Aerospace Engineering,
UCLA,
46-147N EIV,
Los Angeles, CA 90095-1597
e-mail: carman@seas.ucla.edu

The abundance of low-grade waste heat necessitates energy harvesting devices to convert thermal energy to electrical energy. Through magnetic transduction, thermomagnetics can perform this conversion at reasonable efficiencies. Thermomagnetic materials use thermal energy to switch between magnetic and non-magnetic states and convert thermal energy into electrical energy. In this study, we numerically analyzed an active thermomagnetic device for thermal energy harvesting composed of gadolinium (Gd) and neodymium iron boron (NdFeB). A parametric study to determine the device efficiency was conducted by varying the gap distance, heat source temperature, and Gd thickness. Furthermore, the effect of the thermal conductance and applied field was also evaluated. It was found that the relative efficiency for smaller gap distances ranges from ~15% to 28%; the largest allowable volume of Gd should be used and higher applied field leads to higher efficiencies.
[DOI: 10.1115/1.4046273]

Keywords: energy conversion/systems, heat energy generation/storage/transfer, thermomagnetics, multiferroics

Introduction

With an ever-growing need for alternative energy sources, the abundance of thermal energy has spawned an array of conversion technologies for various applications. In 2017, the USA increased its clean energy focus recognizing the waste heat generated by methods such as chemical processing, vehicle operation, or other devices amounted to 66.7 quadrillion BTU.[2] According to Advanced Research Projects Agency-Energy (ARPA-E), for a temperature range of 50–700 °C, nearly 75% of the waste heat is low-grade (≤230 °C). Additionally, assuming a cold side temperature of 25 °C, 45% of the work potential is accessible using low-grade waste heat converted at a Carnot efficiency of ~40% [1]. Therefore, waste heat represents a pervasive form of energy that can be converted into useful electrical energy.

Various thermal conversion technologies have been investigated but thermoelectric (Seebeck) devices remain the primary focus due to their long history of directly transducing temperature gradients to an electric energy [2–4]. Though numerous research efforts investigating Seebeck devices have been conducted, their performance for low-temperature (<100 °C) energy conversion remains limited due to relatively low conversion efficiency of <20% of Carnot and a power conversion efficiency of less than 5% [3]. Another approach that has received modest attention is thermomagnetic devices which convert thermal energy to electrical energy through magnetic transduction [4–22].

Thermomagnetic transduction consists of a system containing a soft magnet and a hard magnet where the soft magnet undergoes a thermally induced second-order ferromagnetic to paramagnetic phase transition. The transition temperature between the phases is known as the Curie point or Curie temperature. Energy is harvested using a passive or active thermomagnetic device [23]. For passive devices, the soft magnet is attached to a piezoelectric material that converts the mechanical oscillations into electricity through a two-step process. The temperature change causes the soft magnet to oscillate between a hot and a cold surface where the hard magnet is located at the hot side with mechanical motion producing electrical energy, i.e., piezoelectric effect. Active devices use a soft magnet as a shunt in a permanent magnet. A coil surrounds the configuration and the thermal transition switches the magnetic field, converting thermal energy directly to electric energy [23] and thus avoids the two-step process in passive devices.

Devices were initially developed and patented in the late 19th century [5,16]. However, it was not until 1948 when Brillouin and Iskenderian determined that thermally oscillating ferromagnetic materials above and below the Curie Point could produce large relative efficiencies (i.e., 55% of Carnot) [8]. The analytical predictions were substantially larger than Seebeck devices, but they required large magnetic fields and did not account for the disorder present in the system when transitioning across the second-order phase transition limiting operating efficiency. In 1959, Elliott et al. experimentally evaluated gadolinium (Gd) for use in a thermomagnetic energy harvesting system operating at room temperature [24]. However, it failed to produce significant power outputs due to the lack of sufficiently strong magnets to bias the structures with high fields.

The advent of high remanence rare earth magnet catalyzed further development. In the 1980s and early 1990s, several device iterations were developed to increase efficiency bias field variance or through regeneration [6,9,13]. More recently, Ujihara et al. developed a strain mediated multiferroic device for thermal to electrical transduction using Gd [12] relying on a two-step process that requires piezoelectric springs for transduction from thermal to electrical energy. This particular device was evaluated for power generation rather than efficiency. Later, Bulgrin et al. analytically optimized Ujihara's device and determined that the usage of ferromagnetic materials which transition over smaller temperature intervals increases the efficiencies [10]. Furthermore, Hsu experimentally evaluated poly-crystalline Gd and analytically postulated that using nanoscale single domain Gd elements could increase relative efficiencies to 30% of Carnot [25]. Chun et al. further developed a thermo-magneto-electric generator and evaluated the device for waste heat recovery from a central processing unit and reported promise in electricity generation as well as heat dissipation (cooling) [22].

In this study, an active thermomagnetic device, which directly transduces thermal to electrical energy, was developed using a finite element analysis (FEA) model. The model was numerically evaluated based on several device parameters that affect operational

efficiency for low-grade waste heat recovery [10,21]. The focus of this study centers on the effects of operational conditions assuming maximum transduction efficiency. The transduction efficiency is the conversion of thermal energy to magnetic energy and is strongly sensitive to material selection and processing [15]. The maximum transduction efficiency is used to decouple the materials' conversion ability due to processing from its performance through varying external operational conditions. Thus, the lens is placed on the conversion of thermal to electrical energy using a highly efficient material.

Parametric studies varying the distance between the hot and cold sources, the hot source temperature and the thickness of Gd for applied magnetic field, and normal and enhanced contact conductance were used to assess their impact on efficiencies. The conclusion of this study found that the development of a device with the smallest gap distance, while utilizing the largest volume of ferromagnetic material that operates with a Curie temperature close to the hot source temperature, is optimal for increasing the thermal to magnetic efficiencies.

Thermomagnetic Device Model Development

This active energy harvesting system is based on the motion of the ferromagnetic material within a solenoid coil as illustrated in Fig. 1. The mechanical motion of the ferromagnetic material coupled with its magnetic changes during this motion produces electrical current in the coil which can be harvested. The system modeled in this study consists of a ferromagnetic material, Gd, a neodymium iron boron (NdFeB) permanent magnet, a solenoid coil, mechanical springs, and a hot/cold source.

As seen in Fig. 1(a), the ferromagnetic Gd is attached to mechanical springs connected to the cold source at the bottom of the figure. The duty cycle of the device is explained with the four stage process illustrated in Fig. 1(b) representing a cross section of Fig. 1(a). In stage I, the Gd is at room temperature and in contact with the cold surface to initiate the thermal energy harvesting cycle. At room temperature, the Gd is below the Curie temperature T_c and is thus ferromagnetic. At this temperature, the dipolar fields attract the Gd to the NdFeB permanent magnet. In stage II, the magnetic force between the Gd and NdFeB exceeds the spring forces and any gravitational forces to translate the Gd toward the NdFeB permanent magnet. In accordance with Faraday's law, this movement generates a voltage within the surrounding coil. At stage III,

the Gd is in contact with the hot side and is heated above the T_c to become paramagnetic. At stage IV, the spring and gravitational forces exerted on the Gd exceed the magnetic force (i.e., Gd is paramagnetic at this stage) and the Gd moves toward the cold source.

The above energy harvesting system was analyzed using COMSOL 5.1 with a FEA model using a 2D axisymmetric approach as shown in Fig. 2(a). A 360-deg revolution of the 2D axisymmetric model results in the 3D formation (Figs. 2(b) and 2(c)). Triangular mesh elements were used for every domain except the air gap above and below the Gd, as seen in Fig. 3. The air gap contains a mapped mesh with rectangular elements that allows for expansion and compression during the movement of the Gd domain. A smaller element size is assigned to the vertical boundary between the coil and the NdFeB/Gd/C domains. The smaller element size increases numerical accuracy at the interface due to large gradient terms. A time-dependent, fully coupled study was used with the PARDISO solver.

A convergence study was used to determine the appropriate element sizes for all regions. This multiphysical model couples heat transfer, magnetostatics, and kinematic equations to determine the effects of the designated thermal cycle on voltage generation in the coil, i.e., electrical energy produced. Thermally insulated boundaries are included on the exterior borders of the model. The model is assumed to be in a vacuum. Therefore, convective heat transfer is removed. Radiative heat transfer is negligible compared to the main interactions of the Gd with the heat sources. Assumptions include a uniform generated magnetic field produced by the NdFeB magnet, hot/cold sources temperatures constant, and linear springs. The springs are not physically present in the 2D axisymmetric model but are assigned to the appropriate domain using kinematic equations. Additionally, thermal and magnetic hystereses are not included in this model. Model validation was conducted through a frequency comparison with the experimental work conducted by Ujihara et al. Though the designs are different (active versus passive), the frequency response driven by the thermal cycle and springs can be compared. However, a large size reduction of this model would require a large deviation from the intended model design. Therefore, the geometric and thermal properties of this model were configured to match the specifications of the experimental work at the largest gap distance. The exponential trend of the experimental frequency within a vacuum follows the trend:

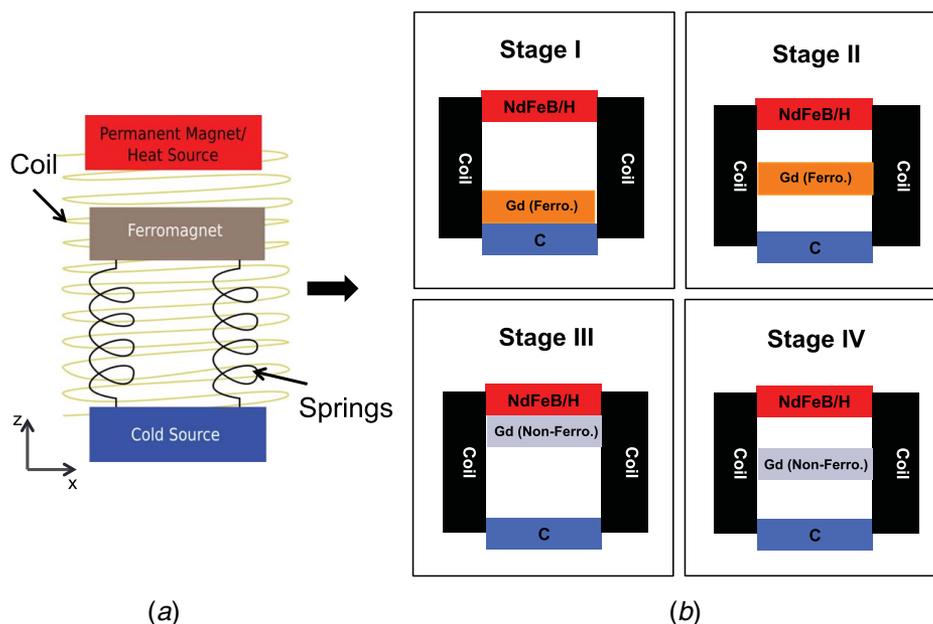$$y = 1.6607x^{-0.949} \qquad (1)$$

(a)   (b)

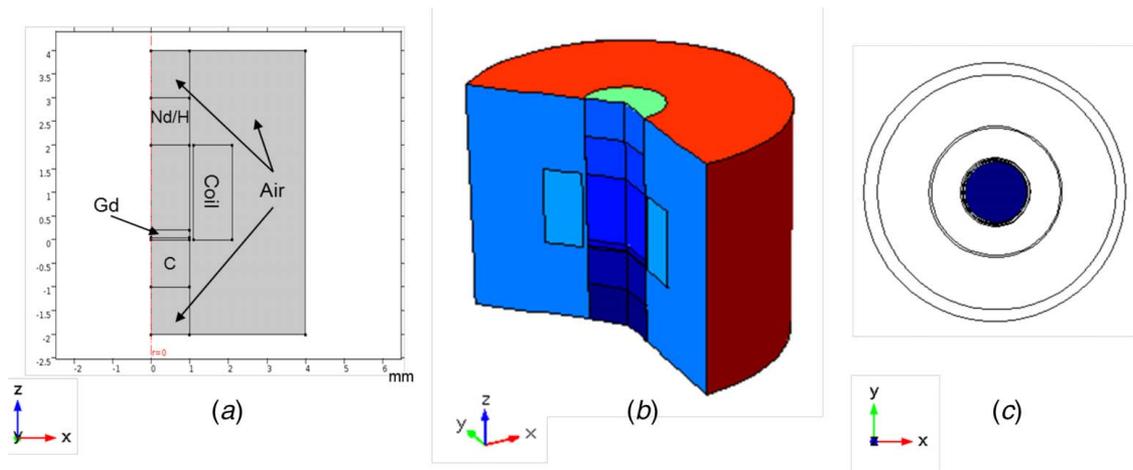**Fig. 1** (a) Thermomagnetic device schematic and (b) operation stages

Fig. 2 Model of the thermomagnetic device. (a) 2D axisymmetric view, (b) 3D view, and (c) 3D top view where the colored circle is in the top cross-sectional area of Gd.

At the largest gap distance, the frequency error between the model and experimental data is an acceptable ∼6%. To fully validate and calibrate the model, experimental work would need to be conducted. The forces acting on the Gd dictate the position and thus the energy harvested during the process. The forces can be represented as

$$F = F_g + F_s + F_{mag} \qquad (2)$$

where the gravitational force, F_g, is negligible and is not considered in this modeling. The spring force F_s is expressed as

$$F_s = -k \cdot z \qquad (3)$$

where z is the vertical distance from the cold source to the heat source and k is the spring constant. At the top of the cold surface, $z = 0$. The magnetic force, F_{mag}, is

$$F_{mag} = \int_V \nabla(MB_{ext}) \qquad (4)$$

where a volume integral is used to determine the force as a function of the magnetization M of Gd and the total external magnetic flux density from the permanent magnetic, B_{ext}. The magnetic state for NdFeB is pointing in the z direction and the hot temperature is selected to be above Gd T_c. For the Gd, the magnetic moments are aligned with magnetic moments applied from the Nd magnet (z direction) but these magnetic moments are a function of temperature. The expansion of (3) to account for surface and volume magneto effects in the z direction by Joshi reduces to

$$
\begin{aligned}
&F_{mag}(z) \\
&= -A_{Gd}\int_{b^-}^{b^+} \frac{dM}{dz} \cdot B_{ext}(z)\, dz + A_{Gd}M(z)\int_{b^-}^{b^+} \frac{dM}{dz} \cdot B_{ext}(z) - M_{b^-} \cdot B_{ext(b^-)}
\end{aligned}
$$
$$(5)$$

where A is the top cross-sectional area (Fig. 2(c)) of the Gd and b is the upper (+) or lower (−) boundary of the Gd. The Gd magnetization as a function of temperature was extracted from and experimental data by Dan'kov and incorporated in the model using the Gd M-H-T graph are shown in Fig. 4 [26].

In this dynamic model, damping was introduced to reduce/eliminate vibration when the Gd reaches the stopping points, i.e., hot and cold surfaces. An underdamped ratio was selected and represented as

$$D = 0.4\sqrt{4 \cdot m \cdot k} \qquad (6)$$

where m is the mass of the Gd and D is the damping coefficient.
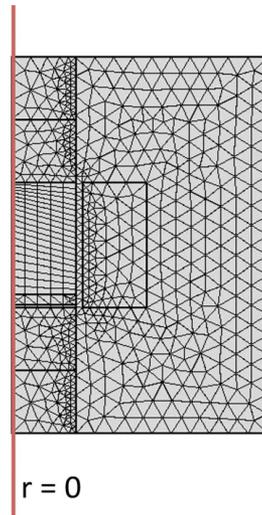

Fig. 3 Meshed 2D axisymmetric view

The dynamic motion of the Gd is represented as

$$m \cdot \frac{dv}{dt} + D \cdot v + k \cdot z = F_{mag}(z, v, t) \qquad (7)$$

where the velocity, v, was computed using the magnetic force and position of the Gd. The amount of electrical energy generated is determined by

$$V_{gen} = -NA\left(\frac{dB}{dt}\right) \qquad (8)$$

where V_{gen} is the voltage generated, N is the number of coil turns, A is the area of the coil, and dB/dt corresponds to the changing magnetic field as a function of time.

The average power (P_{avg}) is determined using [18]

$$P_{avg} = \frac{V_{avg}^2}{2\Omega} \qquad (9)$$

where V_{avg} is calculated through the average of V_{gen} per cycle and Ω is the coil resistance.
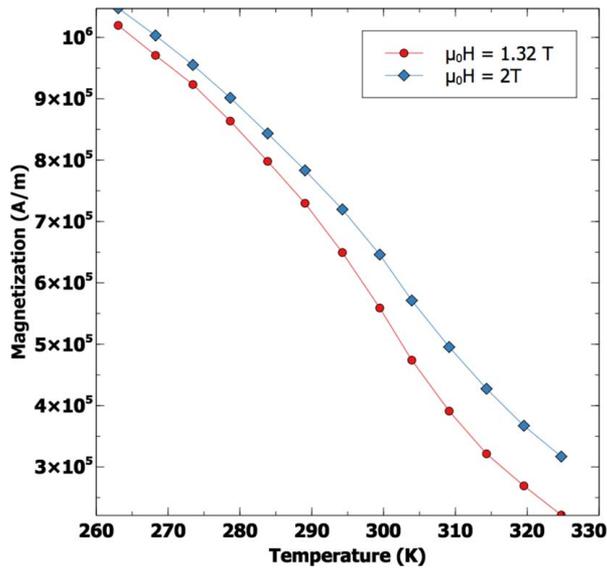
Fig. 4 Magnetization of a gadolinium as a function of field at various temperatures [26]

The heat input (Q_{in}) is determined from

$$Q_{in} = \int_{t}^{t+\Delta t} mc(T_H - T_o)dt \qquad (10)$$

where t is the time at the beginning of the cycle, Δt is the duration of the cycle, m is the Gd mass, c is the Gd specific heat, T_H is the temperature of the heat, and T_o is the initial temperature of the Gd.

The absolute efficiency of the device is calculated by combining Eqs. (9) and (10) to yield

$$\eta_{abs} = \frac{P_{avg}}{Q_{in}} \qquad (11)$$

Thus, the relative efficiency (i.e., to Carnot) is defined as

$$\eta_{rel} = \frac{\eta_{abs}}{\eta_{carnot}} = \frac{P_{avg}}{Q_{in}} * \frac{T_H}{T_H - T_C} \qquad (12)$$

An overview of the parametric study performed is shown in Fig. 5. The base model was designed using typical geometry (gap distance, Gd thickness) and operational (contact conductance, applied field, heat source temperature) inputs. The first parametric study was compared using a 1.32 T versus 2 T NdFeB generated applied field. The second parametric study compared the normal versus enhanced contact conductance. The influence of gap distance
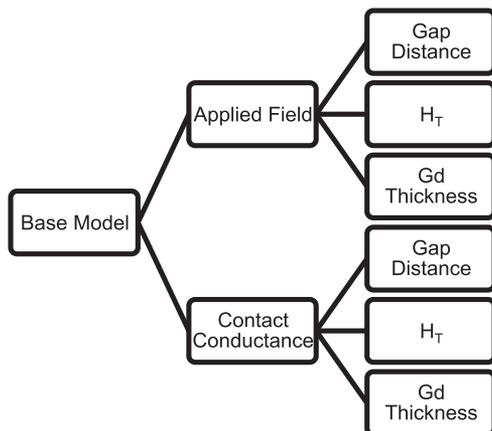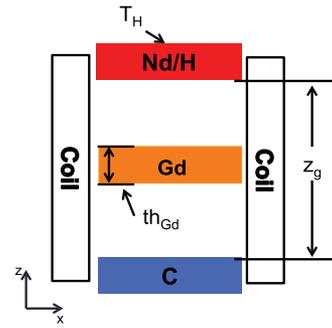

Fig. 5 Overview of parametric studies

Fig. 6 Schematic of study evaluation areas

Table 1 Model inputs

	Base	Range
Gap distance (mm)	2	1–2
Gd thickness (mm)	0.1	0.1–1.0
Gd initial temperature (K)	286	–
Heat source (K)	300	300–320
Heat sink (K)	285	–
Spring constant (N/m)	1	–
# of coil turns	800	–
Applied field (T)	1 (normal)	2 (enhanced)
h (W/m^2 K)	650 (normal)	2×10^3 (enhanced)
Ω[ohms]	10.53	10.53

(z_g), thickness of the Gd (th$_{Gd}$), and hot source temperature (T_H) was evaluated for each parametric study as well as the influence on efficiency.

Figure 6 defines the parameters in the base model (z_g, th$_{Gd}$, T_H) with specific values studied provided in Table 1. A range for each evaluation area was investigated for the normal and enhanced contact conductance and 1.32 T/2 T applied field. The typical contact conductance between NdFeB and Gd (650 W/(m^2 K)) was reported [10], and in this study, we use an enhanced contact conductance (2000 W/(m^2 K)) to represent thermal interface materials such as carbon nanotubes or heat spreaders [27]. The contact resistance was applied to the boundary between the heat source and Gd as well as the boundary between the Gd and heat sink using Eqs. (13) and (14), respectively.

$$q_{H/Gd} = -h(T_{Gd} - T_H) \qquad (13)$$

$$q_{Gd/C} = -h(T_C - T_{Gd}) \qquad (14)$$

where $q_{H/Gd}$ is the heat flux between the heat source and Gd, $q_{Gd/C}$ is the heat flux between the Gd and the heat sink, h is the contact conductance, and T are the temperatures for the corresponding boundary. Additionally, it has been shown that applied field variance can increase voltage generation [13] so the applied field of the NdFeB magnet (1.32 T) was compared to a superconducting magnet (2 T). Geometric aspects influence energy density and incorporation within the harvesting cycle, thus the gap distance and Gd thickness were also varied. Though Gd has a Curie temperature of 293 K [28], methods to increase Curie temperatures through material layering or alloying are possible [20,29]. Thus, the influence of heat source temperature variance and Curie temperature on device efficiency was also evaluated.

Results and Discussion

Prior to discussing the study results, it is helpful to understand representative outputs from the model. Figure 7 plots Gd position
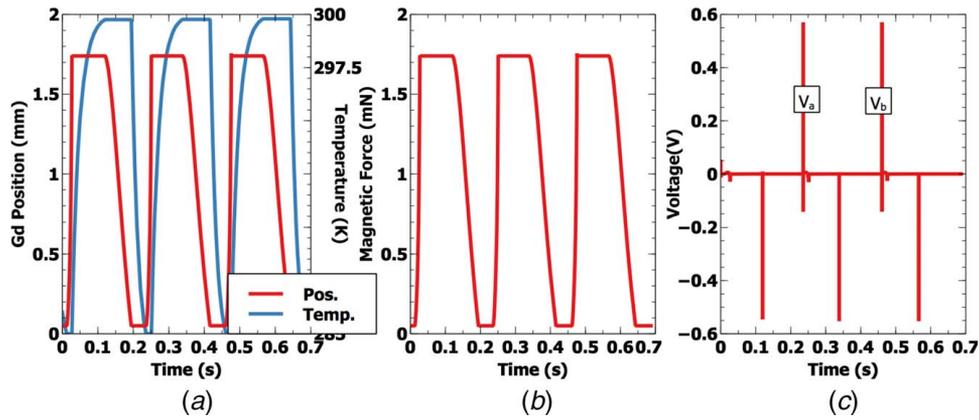
Fig. 7 (*a*) Gd position and temperature versus time, (*b*) magnetic force felt by Gd versus time, and (*c*) voltage generated versus time

and temperature versus time, magnetic force versus time, and voltage versus time from a model simulated using the base properties in Table 1. These data were collected and used to determine the frequency, power, and relative efficiency per cycle. In Fig. 7(*a*), when the position is 0 mm, the lower boundary of the Gd was in contact with the heat sink. Then, the Gd moved from the heat sink to the heat source, stopping at the heat source. In Fig. 7(*a*), the Gd stopped at 1.75 mm, where the top boundary of the Gd was in contact with the heat source. Once the Gd reached the heat source, its temperature increased (i.e., $T = 299$ K) near the Curie temperature and the magnetization approached "0" allowing the Gd to return to the heat sink. The effects of the changes in magnetization can be seen closer in Fig. 7(*b*). The magnetic force is dependent upon the magnetization of the Gd which is dependent on the temperature of the Gd. Initially, the temperature of the Gd is below the Curie temperature which enables full magnetization. This magnetization contributes to the magnetic force (as described in Eq. (5)) which attracted mechanically the Gd toward the NdFeB heat source. The heating of the Gd increased the temperature to the Cure temperature, where the magnetization reached "0" and subsequently the magnetic force decreased to 0 mN. The spring force restored the Gd to the heat sink. As can be seen in the figures, the system exhibits a delay in the initialization of the return to the heat sink due to remanence magnetization.

The Gd movement induces a voltage in the coil as a function of time as shown in Fig. 7(*c*). When the Gd moved toward the heat source, a positive voltage was generated. The distance between two voltage peaks represents one complete cycle. The time was determined at each max voltage peak and Eq. (15) was used to determine the frequency for each cycle.

$$f = \frac{1}{(t_{\text{at }V2} - t_{\text{at }V1})} \qquad (15)$$

The case results for frequency, power, and relative efficiency are displayed in the remainder of this section. For the applied field parametric study, the case results will be referred to as 1.32 T or 2 T. For the contact conductance parametric study, the case results will be referred to as NORMAL or ENHANCED. As a reminder, the parameters used in the studies are presented in Table 1.

Frequency

Figure 8 displays the frequency versus the three parameters (1) gap distance (z_g), (2) hot source temperature (T_H), and (3) Gd thickness (th$_{Gd}$) for both applied fields and both contact conductance cases. Though frequency was calculated from voltage induction, it was dependent on the thermal cycle. An inverse correlation between frequency and each parameter (z_g, T_H, and th$_{Gd}$) was expected. The increase in z_g increased the distance between the heat source and

the sink, and thus a longer thermal cycle, which leads to a lower frequency. In Fig. 8(*a*), this occurred for the 1.32 T case, and the 2 T case showed a resonant frequency at the gap distance of 1.75 mm. Generally, when operating at the resonant frequency, power generation for a given time duration increases due to an increase in the number of cycles [7]. However, the magnitude of the voltage generated is still magnetic field gradient dependent. Additionally, the emergence of the resonant frequency for the 2 T and absence for the 1.32 T case gives insight to a correlation between the gap distance, Gd volume, and applied field. This information could possibly foreshadow the scalability of the device. Further investigation is needed to determine the extent of its relevance and relationship to efficiency. As the T_H increased, the heat flux into the Gd was increased and the magnetic force decreases similarly, increasing the cycle duration. The larger cycle duration is directly responsible for reducing the frequency. Figure 8(*b*) displays the frequency for 1.32 T and 2 T as a result of that performance. A reduction in th$_{Gd}$ decreased the time it took the magnetic material shuttled through the coil but it also reduced the thermal cycle. The reduced thermal cycles result in a net increase in frequency. This is observed in Fig. 8(*c*) for both 1.32 T and 2 T. They both had the same frequencies except at the smallest th$_{Gd}$. This could be due to the existence of a minimal amount of magnetic material within the 0.25–0.1 mm range for each applied field.

Furthermore, Ujihara et al. and Bulgrin et al. have demonstrated that increasing the contact conductance will increase the frequency. In Fig. 8(*d*), as the Z_g increased, the frequency for ENHANCED is higher (as expected) but decreased (~18.3%) compared to (~10.5%) for NORMAL. ENHANCED decreased almost two times faster because the higher contact conductance affects the thermomagnetic cycle by increasing the rate of thermal activation. Thus, the thermal activation driven by the heat source and heat sink is more sensitive to the distance between them. The frequencies for NORMAL and ENHANCED (Fig. 8(*e*)) were the highest at $T_H = 300$ K or 305 K, respectively, and decreased with minimal inflections as the temperature increased. This behavior is evident of the need for T_H to be selected as close to the Curie temperature as possible to ensure a higher frequency. Additionally, a high contact conductance will allow operation at a higher temperature but within certain limits. Determining the optimal temperature operation range as a function of contact conductance could represent the next steps in device design. ENHANCED had a higher frequency than NORMAL at each thickness but with the same correlation. ENHANCED had the highest frequency for each parameter further exemplifying the influence of contact conductance on generating higher frequency. However, th$_{Gd}$ had the largest range for each comparison case (~2.5 to 6 Hz for ENHANCED and ~1 to 4 Hz for NORMAL). The magnetic force is dictated by the th$_{Gd}$. Though a reduction in thickness means a reduction in magnetic material and thus magnetic force, influencing the travel velocity,
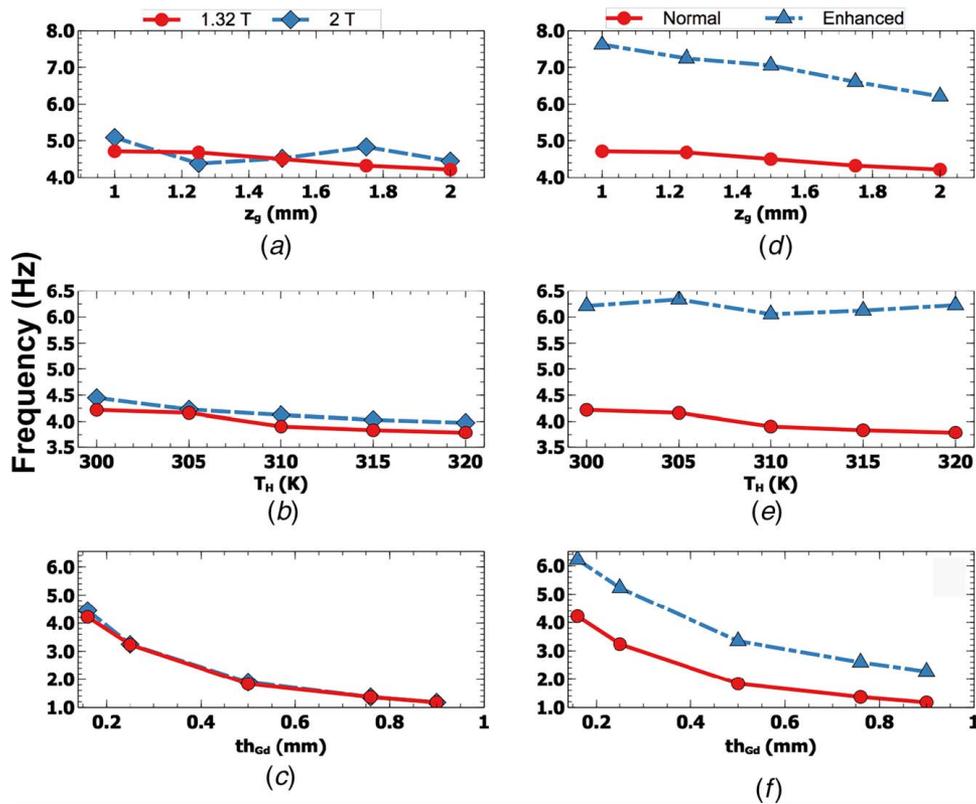
Fig. 8 Frequency versus gap distance, heat source temperature, and Gd thickness for (a)–(c) the applied field study and (d)–(f) the contact conductance study

it also means faster conduction. This can be seen clearly in Fig. 8(f) as ENHANCED was a combination of higher conduction and contact conductance. Overall, the contact conductance is more influential than the applied field in targeting higher frequencies. Moreover, smaller z_g values lead to higher frequencies.

Power

Figure 9 provides plots of power versus the parameters (gap distance (z_g), hot source temperature (T_H), and Gd thickness (th$_{Gd}$)) for the applied field and contact conductance cases. Power and gap distance are inversely correlated to an increase in z_g. The applied field case demonstrated that an increase in magnetic field generated more power while the contact conductance case was less definitive which differs from the frequency response. All the 2 T cases generated higher power than the applied 1.32 T case. In Fig. 9(a), the largest difference in power occurred at the smallest z_g and the smallest difference occurred at the largest z_g. The applied magnetic field had more influence at smaller distances. Figure 9(b) shows maxima T_H at 305 K and 310 K for 1.32 T and 2 T, respectively. This higher power is attributed to either an extension of the ferromagnetic region, a decrease in frequency or both. However, it can be observed that 2 T case increased the power output by ~128%. The larger th$_{Gd}$ had the highest power generation due to the larger amount of magnetic material that is critical to voltage generation.

In Figs. 9(d) and 9(f), the power output is nearly the same for NORMAL and ENHANCED. The power steadily declines until the 1.5 mm distance (Fig. 9(d)). When z_g is larger than 1.5 mm, the correlation weakened. For the T_H, NORMAL had a maxima at 305 K and the power generation for ENHANCED increased after 310 K. The ENHANCED case exhibits a slight frequency increase after 310 K, which provides a bump in the power generation. The power output increased by ~14% compared to the NORMAL case. This further leads to the concept that increased frequency can increase power generation and it also demonstrates the

possibility of expanding the heat source temperature at which the device operates. Similar to the applied field case, the largest th$_{Gd}$ had the highest power generation. Overall, the conclusion remains that higher applied fields generate higher power.

Relative Efficiency

Figure 10 plots the relative efficiency versus the parameters (gap distance (z_g), hot source temperature (T_H), and Gd thickness (th$_{Gd}$)) for the two applied field and two contact conductance cases. The relative efficiency for both cases is inversely related to z_g, T_H, and th$_{Gd}$. The efficiency values for z_g follow a similar same trend as the gap distance cases observed in power generation (Figure 9). In Fig. 10, the 2 T case had the highest efficiency for all parameters studied compared to the lower 1.32 T case. Figures 10(a)–10(c) show relative efficiencies of ~28% for the smallest z_g, and ~8% for both 300 K T_H as well as 0.1 mm th$_{Gd}$. However, for all three plots (Figs. 10(a)–10(c)), the efficiency decreases as the parameters increase. Furthermore, the effective efficiency differences between 1.32 T and 2 T for these three parameters decrease as the parameters increase. These results clearly show the benefits of electing a higher magnetic field in conjunction with other parameters to maximize the efficiency outcomes.

Comparatively, the magnitudes and trend of NORMAL versus ENHANCED conductance (Fig. 10(d)) for z_g were nearly equal. For T_H (Fig. 10(e)), NORMAL and ENHANCED had the same efficiency at 310 K but NORMAL was more efficient at temperatures below 310 K and ENHANCED was more efficient at temperatures above 310 K due to power generation. For th$_{Gd}$, NORMAL and ENHANCED had nearly the same efficiency for each th$_{Gd}$ except 0.1 mm. Additionally, as observed in Fig. 10(f), each case reached a point where efficiency stopped decreasing as th$_{Gd}$ increased. The minimum in Fig. 10(f) can be regarded as the minimum relative efficiency for both conductance cases. The minimum relative efficiency can be used to help curate design specifications based on a balance
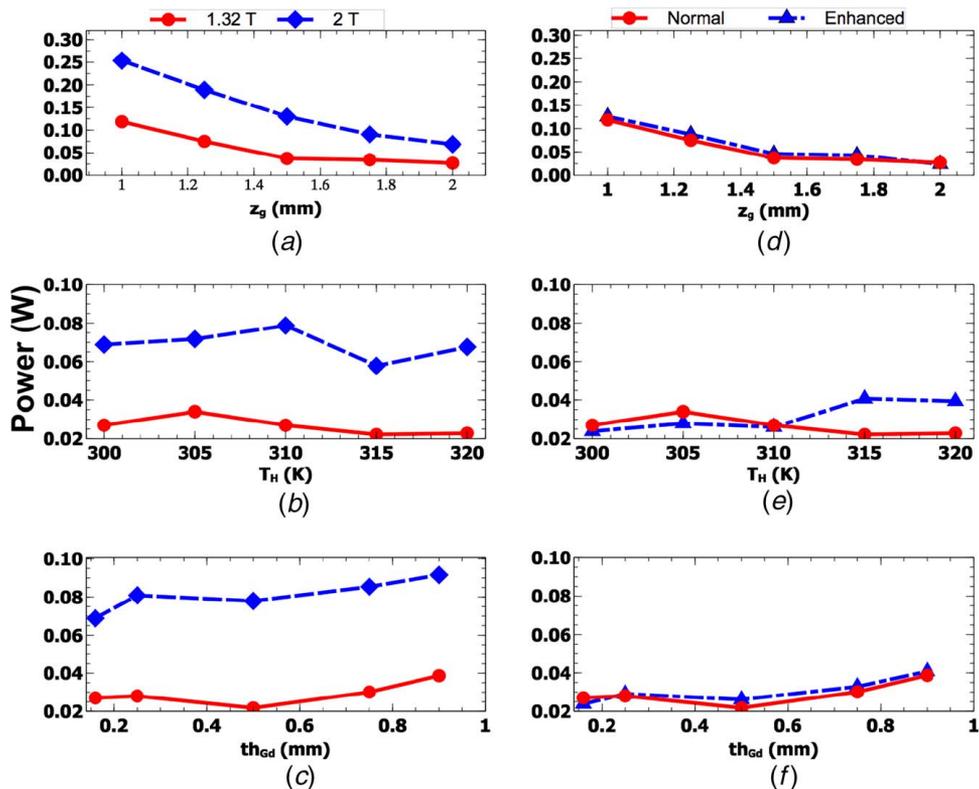
Fig. 9 Power versus gap distance, heat source temperature, and Gd thickness for (a)–(c) the applied field study and (d)–(f) the contact conductance study
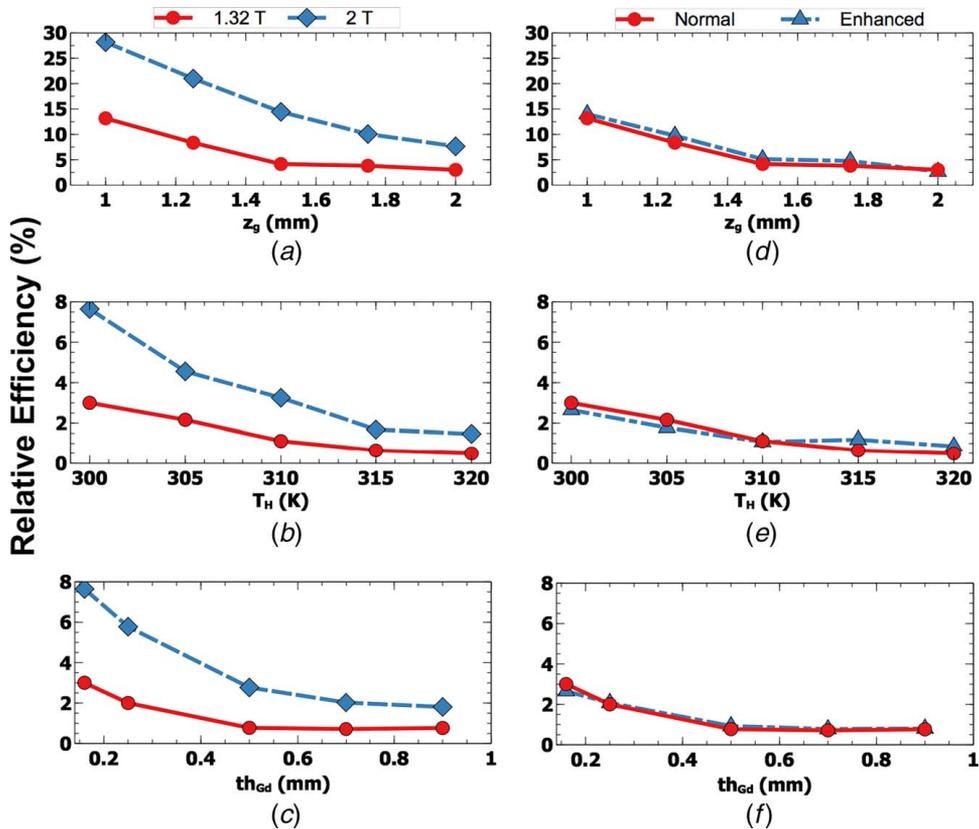

Fig. 10 Relative efficiency versus gap distance, heat source temperature, and Gd thickness for (a)–(c) the applied field study and (d)–(f) the contact conductance study

between compact design, desired power output, and efficiency. Overall, gap distance had a much larger influence on relative efficiency than T_H and th$_{Gd}$. However, a higher applied field was more important to achieve higher efficiencies.

The parametric studies revealed the influence of key design features on device operation. The z_g is the more dominant feature. As the z_g reduces, more power is generated due to a reduction in travel time. The T_H remains stationary as the gap distance changes. Therefore, we determined that the efficiency is dominated by the power. The culmination of each study framed an optimal device that operates close to its Curie temperature and consists of a smaller gap distance with a larger volume of Gd to achieve higher efficiencies. The amount of power reported in Fig. 9 is sufficient for low power devices such as wearables. Additionally, we found that the higher applied field is more important than the enhanced contact conductance. Though the enhanced contact conductance leads to higher frequencies, a higher applied field generates more power/efficiency in the thermomagnetic device. This differs from passive devices where higher contact conductance equates to higher frequencies and thus larger power generation. This is attributed to the coupling of the magnetic force directly to voltage induction. Whereas in a passive device, the mechanical response induces voltage. Further optimization will be achieved through incorporating hysteresis, additional ferromagnetic materials, atomistic thermal transition, and other losses.

Conclusion

This study explored the design aspects of an active thermomagnetic device used to transduce thermal energy to electrical energy. The base system consisted of a NdFeB hard magnet and a Gd soft magnet as the working material that oscillated between a heat sink and a heat source. A parametric study was conducted to understand the effects of varying the gap distance (z_g), heat source temperature (T_H), and Gd thickness (th$_{Gd}$). It was found that when selecting a design, the z_g should be as small as possible and include the largest volume of Gd possible. A higher applied field will achieve favorable efficiencies but should be balanced with an enhanced contact conductance. Additionally, the Curie temperature of the chosen soft magnet should be close to the operating temperature. Future work will include determining the effect of spin reorientation on device efficiency and experimental work to fully assess the promise of this technology.

Acknowledgment

References

[1] ARPA-E, DE, 2016, "Request For Information on Lower Grade Waste Heat Recovery DE-FOA-0001607."
[2] Snyder, G. J., and Ursell, T. S., 2003, "Thermoelectric Efficiency and Compatibility," Phys. Rev. Lett., **91**(14), p. 148301/1.
[3] Zhang, X., and Zhao, L.-D., 2015, "Thermoelectric Materials: Energy Conversion Between Heat and Electricity," J. Mater., **1**(2), pp. 92–105.
[4] Elsheikh, M. H., Shnawah, D. A., Sabri, M. F. M., Said, S. B. M., Haji Hassan, M., Ali Bashir, M. B., and Mohamad, M., 2014, "A Review on Thermoelectric Renewable Energy: Principle Parameters That Affect Their Performance," Renew. Sustain. Energy Rev., **30**, pp. 337–355.
[5] Tesla, N.,1889, Thermo-Magnetic Motor, Patent No: 396121.
[6] Kirol, L. D., and Mills, J. I., 1984, "Numerical Analysis of Thermomagnetic Generators," J. Appl. Phys., **56**(3), pp. 824–828.
[7] Kishore, R. A., and Priya, S., 2017, "Low-Grade Waste Heat Recovery Using the Reverse Magnetocaloric Effect," Sustain. Energy Fuels, **1**(9), pp. 1899–1908.
[8] Elliott, J. F., 1959, "Thermomagnetic Generator," J. Appl. Phys., **30**(11), pp. 1774–1777.
[9] Solomon, D., 1991, "Design of a Thermomagnetic Generator," Energy Convers. Manage., **31**(2), pp. 157–173.
[10] Bulgrin, K. E., Sungtaek Ju, Y., Carman, G. P., and Lavine, A. S., 2009, "A Coupled Thermal and Mechanical Model of a Thermal Energy Harvesting Device," Proceedings of the ASME 2009 International Mechanical Engineering Congress & Exposition, Lake Buena Vista, FL, pp. 327–335.
[11] Stauss, H. E., 1959, "Efficiency of Thermomagnetic Generator [13]," J. Appl. Phys., **30**(10), pp. 1622–1623.
[12] Ujihara, M., Carman, G. P., and Lee, D. G., 2007, "Thermal Energy Harvesting Device Using Ferromagnetic Materials High Temperature Thermoreflectance Imaging and Transient Harman Characterization of Thermoelectric Energy Conversion Devices Feasibility Analysis and Proof of Concept for Thermoelectric Energy," J. Appl. Phys, **91**(107), p. 093508.
[13] Solomon, D., 1988, "Improving the Performance of a Thermomagnetic Generator by Cycling the Magnetic Field," J. Appl. Phys., **63**(3), pp. 915–921.
[14] Srivastava, V., Song, Y., Bhatti, K., and James, R. D., 2011, "The Direct Conversion of Heat to Electricity Using Multiferroic Alloys," Adv. Energy Mater., **1**(1), pp. 97–104.
[15] Wetzlar, K. P., Keller, S. M., Phillips, M. R., and Carman, G. P., 2016, "A Unifying Metric for Comparing Thermomagnetic Transduction Utilizing Magnetic Entropy," J. Appl. Phys., **120**(24), p. 244101.
[16] Edison, T.,1892, Pyromagnetic Generator, Patent No: 380100.
[17] Hsu, R. C. J., Wetzlar, K. P., and Carman, G. P., 2012, "Nanoscale Based Thermal Magnetic Energy Harvesting," Presented at the 2nd Multifunctional Materials for Defense Workshop in Conjunction With the 2012 Annual Grantees'/Contractors' Meeting for AFOSR Program on Mechanics of Multifunctional Materials & Microsystems, Arlington, VA, July 30–Aug. 3, pp. 1–23.
[18] Christiaanse, T., and Brück, E., 2014, "Proof-of-Concept Static Thermomagnetic Generator Experimental Device," Metall. Mater. Trans. E, **1**(1), pp. 36–40.
[19] Lionte, S., Vasile, C., and Siroux, M., 2015, "Numerical Analysis of a Reciprocating Active Magnetic Regenerator," Appl. Therm. Eng, **75**, pp. 871–879.
[20] Vuarnoz, D., Kitanovski, A., Gonin, C., Borgeaud, Y., Delessert, M., Meinen, M., and Egolf, P. W., 2012, "Quantitative Feasibility Study of Magnetocaloric Energy Conversion Utilizing Industrial Waste Heat," Appl. Energy, **100**, pp. 229–237.
[21] Joshi, K. B., and Priya, S., 2013, "Multi-Physics Model of a Thermo-Magnetic Energy Harvester," Smart Mater. Struct., **22**(5).
[22] Chun, J., Song, H. C., Kang, M. G., Kang, H. B., Kishore, R. A., and Priya, S., 2017, "Thermo-Magneto-Electric Generator Arrays for Active Heat Recovery System," Sci. Rep., **7**(1), p. 41383.
[23] Kishore, R. A., and Priya, S., 2018, "A Review on Design and Performance of Thermomagnetic Devices," Renew. Sustain. Energy Rev., **81**, pp. 33–44.
[24] Elliott, J. F., Legvold, S., and Spedding, F. H., 1955, "Magnetic Properties of Erbium Metal," Phys. Rev., **100**(6), pp. 1595–1596.
[25] Hsu, C. J., Sandoval, S. M., Wetzlar, K. P., and Carman, G. P., 2011, "Thermomagnetic Conversion Efficiencies for Ferromagnetic Materials," J. Appl. Phys., **110**(12), p. 123923.
[26] Dan'kov, S. Y., Tishin, A., Pecharsky, V., and Gschneidner, K., 1998, "Magnetic Phase Transitions and the Magnetothermal Properties of Gadolinium," Phys. Rev. B—Condens. Matter Mater. Phys., **57**(6), pp. 3478–3490.
[27] Saviers, K. R., Hodson, S. L., Fisher, T. S., Salvador, J. R., and Kasten, L. S., 2013, "Carbon Nanotube Arrays for Enhanced Thermal Interfaces to Thermoelectric Modules," J. Thermophys. Heat Transfer, **27**(3), pp. 474–481.
[28] Martin, D. H., 1967, *Magnetism in Solids*, MIT Press, Boston, MA.
[29] Parakkat, V. M., Ganesh, K. R., and Anil Kumar, P. S., 2016, "Tailoring Curie Temperature and Magnetic Anisotropy in Ultrathin Pt/Co/Pt Films," AIP Adv., **6**(5), p. 56118.